Two-dimensional carbon nitride (2DCN) nanosheets: Tuning of novel electronic and magnetic properties by hydrogenation, atom substitution and defect engineering

Asadollah Bafekry (iD), Saber Farjami Shayesteh (iD), and Francois M. Peeters (iD)

COLLECTIONS

View Online   Export Citation   CrossMark

ARTICLES YOU MAY BE INTERESTED IN

Lock-in Amplifiers
... and more, from DC to 600 MHz
Watch

Two-dimensional carbon nitride (2DCN) nanosheets: Tuning of novel electronic and magnetic properties by hydrogenation, atom substitution and defect engineering

View Online   Export Citation   CrossMark

Asadollah Bafekry,[1,2,a)] [iD] Saber Farjami Shayesteh,[1] [iD] and Francois M. Peeters[2] [iD]

AFFILIATIONS

[1]Department of Physics, University of Guilan, 41335-1914 Rasht, Iran
[2]Department of Physics, University of Antwerp, Groenenborgerlaan 171, B-2020 Antwerp, Belgium

Note: This paper is part of the Special Topic on Defects in Semiconductors 2020.
[a)]**Author to whom correspondence should be addressed:** Asadollah.Bafekry.@uantwerpen.be

ABSTRACT

By employing first-principles calculations within the framework of density functional theory, we investigated the structural, electronic, and magnetic properties of graphene and various two-dimensional carbon-nitride (2DNC) nanosheets. The different 2DCN gives rise to diverse electronic properties such as metals (C_3N_2), semimetals (C_4N and C_9N_4), half-metals (C_4N_3), ferromagnetic-metals (C_9N_7), semiconductors (C_2N, C_3N, C_3N_4, C_6N_6, and C_6N_8), spin-glass semiconductors ($C_{10}N_9$ and $C_{14}N_{12}$), and insulators (C_2N_2). Furthermore, the effects of adsorption and substitution of hydrogen atoms as well as N-vacancy defects on the electronic and magnetic properties are systematically studied. The introduction of point defects, including N vacancies, interstitial H impurity into graphene and different 2DCN crystals, results in very different band structures. Defect engineering leads to the discovery of potentially exotic properties that make 2DCN interesting for future investigations and emerging technological applications with precisely tailored properties. These properties can be useful for applications in various fields such as catalysis, energy storage, nanoelectronic devices, spintronics, optoelectronics, and nanosensors.

I. INTRODUCTION

Recently, a special class of two-dimensional materials (2DM), made from carbon and nitrogen atoms, has attracted much attention due to their outstanding physical and chemical properties. Layered nanomaterials solely composed of C and N atoms, with the ability of N atoms to take many different positions, enhance the possibilities to form strong covalent networks. These features allow to grow an extensive number of graphenic carbon-nitride lattices. Two-dimensional carbon-nitride (2DCN) allotropes show a common chemical formula C_nN_m, where n and m represent the number of C and N atoms in the primitive lattice, respectively. 2DCN nanomaterials are well known to exhibit strong and stable components, owing to the formation of covalent bonds between the C–C and C–N bonds. For different compositions and configurations of the C and N atoms, these nanomaterials can exhibit diverse and promising electronic, optical, mechanical, and thermal properties. 2DCN shows attractive bandgaps and offers surface engineering possibilities and are well known to have interesting application prospects in both energy- and environment-related topics, including catalysts, photocatalysis, and hydrogen evolution.[1–7]

A few decades ago, 2DCN with the chemical formula C_3N_4 was synthesized.[3] Unlike graphite, 2DCN shows porous atomic lattices and more importantly are inherent semiconductors.[8] Very recently, 2D nitrogenated holey graphene with C_2N stoichiometry was experimentally fabricated via a wet-chemical reaction.[9] C_2N, which contains an evenly distributed lattice of N and hole sites, makes it an excellent candidate as a nanofilter and an interesting structure for the adsorption of atoms and molecules.[9,11] Recently, Mahmood *et al.*, reported the first experimental realization of 2D polyaniline with stoichiometric formula C_3N and a graphenelike

TABLE I. The structural, electronic, and magnetic parameters of graphene and 2DCN nanosheets; including lattice constant a; the bond length between C—C atoms (d_{C-C}); the bond length between C—N atoms (d_{C-N}); the diameter of nanopore D_{NP} and the bandgap (E_g). Electronic state is specified as metal (M), semimetal (SM), half-metal (HM), insulator (INS), spin-glass semiconductor (SG-SC), direct semiconductor (SC-di), and indirect semiconductor (SC-ind). The magnetic moment per supercell M_{tot} is also given.

2DCN	a (Å)	E_F (eV)	d_{C-C} (Å)	d_{C-N} (Å)	D_{NP} (Å)	E_g (eV)	M_{tot} (μ_B)
Graphene	2.46	7.15	1.42	…	…	SM	0
C_2N	8.345	7.58	1.457/1.430	1.342	5.503	SC (1.75)-di	0
C_3N	4.861	7.67	1.404	1.403	…	SC (0.4)-ind	0
C_4N	4.775	7.83	1.445	1.443	…	SM	0
C_2N_2	2.350	7.22	1.445	1.443	…	INS (5)	0
C_3N_2	8.70	7.22	1.402/1.511	1.354/1.392	4.254,5.454	SM	0
C_3N_4	4.74	7.21	…	1.323/1.445	2.728	SC (1.45)-di	0
C_4N_3	4.81	7.26	1.427	1.346	2.736	HM (2.2)	1
C_6N_6	7.11	7.35	1.503	1.343	5.447	SC (1.5)-di	0
C_6N_8	7.14	7.27	…	1.414/1.455	4.773	SC (1.22)-in	0
C_9N_4	9.72	7.60	1.428/1.470	1.348/1.407	5.588	SM	0
C_9N_7	8.05	78.30	1.414/1.488	1.385/1.444	5.472	FM	0.8
$C_{10}N_9$	9.86	7.33	1.418/1.502	1.370/1.385	7.300	SG-SC (1.7)	1

structure in which nitrogen is uniformly distributed.[10] Theoretical studies showed that C_3N exhibits ultrahigh stiffness and thermal conductivity.[12] Furthermore, DFT calculations showed that the electronic properties of C_3N can be tuned by the adsorption of atoms and molecules.[12–15] Like its C_2N counterparts, C_3N is also an intrinsic semiconductor according to recent theoretical studies. A C_3N nanosheet can show desirable properties for different applications, like nanoelectronics, catalysis, and hydrogen storage.[16–20]

C_3N_4 showed semiconducting properties with the possibility to be a potential photocatalyst for water splitting.[21,22] This structure features intrinsic vacancies that are expected to produce a spin-polarized state, while the electronic property of C_3N_4 will be drastically modified when atoms are substituted. C_4N_3 is the counterpart of C_3N_4 and is at present the only that has been experimentally synthesized[23] and was identified to be half-metallic.[24] Metal-free magnetism and half-metallicity in C_4N_3 nanosheets and nanotubes[25–27] was recently predicted to be useful in spintronic devices. Recently, C_6N_6 has been explored in experiments[28,29] and was investigated theoretically.[30] It was shown that C_6N_6 has topologically nontrivial electronic states and it can be tuned into a topological insulator by doping.[31] The successful synthesis and fabrication of C_2N, C_3N, C_6N_8, and C_6N_6 through bottom-up procedures motivated us to consider different approaches to tune the bandgap.[3,9,32]

In spite of the fact that 2DM hold great potential for a wide range of applications, it will be necessary to modulate their intrinsic properties to transfer them into real applications. In recent years, several approaches have been developed to modify the electronic and magnetic properties of 2DM. Defects can be generated during the growth and preparation process of the nanomaterial. It is well known that defects are difficult to avoid in materials especially in 2DM, which can dramatically affect the structure, its electronic and magnetic properties, and the performance of 2DM-based devices. Defects are usually seen as detrimental to device performance. However, they also can bring about new beneficial effects on the electronic structure[33,34] and expand the potential applications of

2DM.[35–38] Therefore, it is very important to understand the influence of these defects on their electronic and magnetic properties. Such understanding would also help in creating ideas to control defects and in this way to prepare 2DM with novel properties.

Point defects, including vacancy, impurity, and interstitial atoms, will tailor the electronic properties of 2DM,[39–45,56–59] which can be used for a wide range of applications.[46–55] While there has been limited theoretical studies, an in depth survey of trends across the range of 2DCN nanosheets, with various defects, is still lacking. In the present work, we first performed an extensive study of the structural, electronic, and magnetic properties of pristine 2DCN nanosheets including C_2N, C_3N, C_4N, C_2N_2, C_3N_2, C_3N_4, C_4N_3, C_6N_6, C_6N_8, C_9N_4, C_9N_7, $C_{10}N_9$, and $C_{14}N_{12}$ by using first-principles calculations. In addition, we investigated the effects of point defects including vacancy, adsorption, and substitution of hydrogen on the structure, electronic, and magnetic properties of graphene and 2DCN nanosheets.

II. COMPUTATIONAL METHOD

In this paper, we performed calculations of the electronic structure with geometric optimization, using spin-polarized density functional theory (DFT) as implemented in the OpenMX Package.[60] This code self-consistently finds the eigenvalues and eigenfunctions of the Kohn-Sham equations for the systems under study using norm-conserving pseudopotentials[62] and pseudoatomic orbitals (PAOs).[63,64] In addition, we used the Perdew-Burke-Ernzerhof generalized gradient approximation (GGA) for exchange and correlation.[61] The K points for sampling over the Brillouin zone (BZ) were generated using the Monkhorst-Pack scheme.[65] After convergence tests, we chose different energy cutoffs (for instance, 300 Ry for C_3N) so that the total-energy converge below 1.0 meV/atom. In the first step, the atomic positions are optimized using a quasi-Newton algorithm for atomic force relaxation. The geometries were fully relaxed until the force acting on each atom was less than 1 meV/Å. The Brillouin zone (BZ) is sampled by a K-mesh grid of 23 × 23 × 1

and scaled according to the size of the supercell. The 2DCN is modeled as a periodic slab with a sufficiently large vacuum layer (20 Å) in order to avoid interaction between adjacent layers. Simulated scanning tunneling microscopy (STM) images were obtained using the Tersoff-Hamann theory[66] and were graphed using WSxM software.[67] The formation energy per atom in a primitive unit cell was calculated using the formula $E_F = (N_C E_C + N_N E_N - E_{C_n N_m})/(N_C + N_N)$, where E_C and E_N denote the total energies of the single C and N atoms, respectively, while $E_{C_n N_m}$ denotes the total energy of the different monolayers $C_n N_m$. The formation energies are listed in Table I.

III. PRISTINE 2DCN NANOSHEETS

Geometric atomic structures of graphene and 2DCN nanosheets are shown in Fig. 1. The schematic view of 2DCN nanosheets

including C_2N, C_3N, C_3N_2, C_3N_4, C_4N_3, C_6N_6, C_6N_8, C_9N_4, C_9N_7, $C_{10}N_9$, and $C_{14}N_{12}$ with their various applications are shown in Fig. S1 (see the supplementary material). Before investigating the electronic properties, we first optimize the geometrical structure of 2DCN. The crystal lattice parameters are listed in Table I. The variation of the total energy of the relaxed 2DCN as a function of the crystal lattice constant, with hexagonal and rectangular networks is shown in Fig. S2 of the supplementary material. The optimized geometry for each structure is given as the inset.

The lattice constants of C_2N and C_3N are found to be 8.345 and 4.861 Å, respectively, which are in agreement with previous results.[10,12,14,68–71] For C_2N, $d_{C-N} = 1.342$ Å and $d_{C-C} = 1.429$ and 1.457 Å, while the bond angle of C—N—C is 117°, slightly deviating from 120°. The holey site of C_2N forms a nanopore with a diameter of 5.503 Å.[9] For C_3N, we have $d_{C-C} = 1.404$ Å and $d_{C-N} = 1.403$ Å. C_3N_2 involves two pentagon cores surrounded by
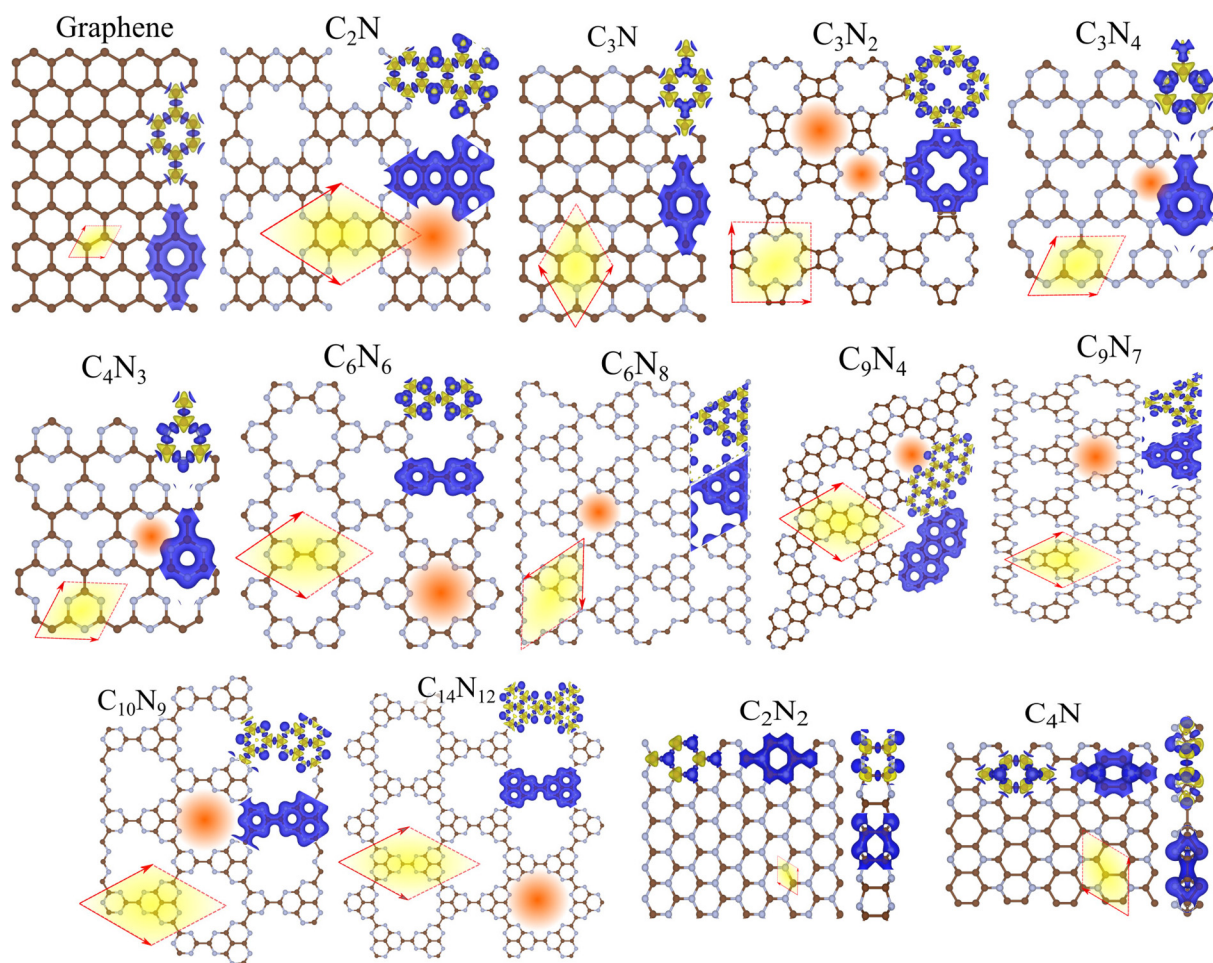

FIG. 1. Geometric structures of graphene and 2DCN nanosheets. A primitive unit cell is indicated by a red parallelogram with total and difference charge densities as shown in the same panel. The blue and yellow regions represent charge accumulation and depletion, respectively, with the brown atoms representing C and the blue atoms representing N. The orange circles represent the regions of nanopores.

C and N atoms and one core surrounded by N atoms and has a lattice parameter of 8.70 Å. The structure is completely planar, in addition we see two nanopores with diameters of 5.545 and 4.254 Å.[72,73] The lattice constant of C_3N_4 (C_4N_3) is calculated to be 4.74 (4.81) Å with $d_{C-C} = 1.323$ (1.427) Å and $d_{C-C} = 1.445$ (1.346) Å.[74] After structural relaxation, the calculated lattice constant for C_6N_6 is 7.11 Å, consistent with previous theoretical and experimental reports.[75–77] The hexagonal nanopore in C_6N_6 has a diameter of 5.447 Å, which is the distance from one N atom to the opposite N atom across the nanopore with a completely planar lattice.[30] C_6N_8 has a lattice constant of 7.14 Å, which is in agreement with previous studies[27,75,78–80] and d_{C-N} can have two values of 1.414 and 1.455 Å.

The structure of C_9N_4 involves 18 C and 8 N atoms, in its unit cell resulting in a geometry similar to C_2N and C_3N so that the unit cell of C_9N_4 is twice that of C_3N by removing another C hexagonal ring, while the N constitutes a honeycomb structure. The lattice constant of C_9N_4 is 9.72 Å and d_{C-C} (d_{C-N}) = 1.348 (1.407) Å. The edge of C_9N_4 nanopore is surrounded by six N atoms in these rings, with diameter of the nanopore of 5.588 Å. These results are in good agreement with previous calculations.[81] The primitive unit cell lattice of C_9N_7 constitutes one center C hexagon ring surrounded by three CN pentagons and has 8.050 Å lattice constant. The d_{C-N} in the pentagons are 1.400 Å and 1.444 Å, which are typical bond lengths for sp^2-hybridization and noticeably smaller than 1.5 Å for standard sp^3-hybridization. The diameter of the nanopore is 5.472 Å. The planar structure and the values of the bond lengths

and bond angles imply that the chemical bonds in C_9N_7 ought to be covalent of character.[82] The lattice constant of $C_{10}N_9$ is calculated to be 9.86 Å and d_{C-C} is 1.502 Å, which is longer than that around the center of the unit cell (i.e., 1.418 Å).[83]

$C_{14}N_{12}$ has a planar 2D structure with a lattice constant of 11.77 Å, and the C—C bond length is 1.435 Å, while the C—N bonds are 1.365 Å with the C—C—C and N—C—N angles equal to 116° and 119°, respectively, which is consistent with the value reported in Refs. 83 and 84. The diameter of the nanopore in $C_{10}N_9$ and $C_{14}N_{12}$ are 7.30 and 9.698 Å, respectively. C_2N_2 is a bilayer structure with a lattice constant of 2.35 Å and interlayer distance $d_{C-C} = 1.443$ Å, and layer thickness of 2.865 Å. The bond angle is comparable with a regular tetrahedral carbon with sp^3-hybridization of 109°, but C_2N_2 shows a slight deviation from the standard tetrahedral carbon structure. The interlayer coupling is strong and is different from the weak van der Waals (vdW) coupling. By adsorbing C atoms on all the N atoms of the monolayer C_3N, one obtains C_4N. The lattice constant of C_4N is 4.77 Å and d_{C-C} (d_{C-N}) is 1.443 (1.343) Å. The C_4N ring is not a regular hexagon since the C—N—C and N—C—N angles are equal to 114° and 125°, respectively. These results are in good agreement with previous theoretical reports.[85] This structure with nanopores can be used as a material with reactive regions inside and thereby is optimal for functionalization by adatoms or molecules.

The total and difference charge density are shown in Fig. 1, in the same panel, where the blue and yellow regions represent the charge accumulation and depletion, respectively. From the difference
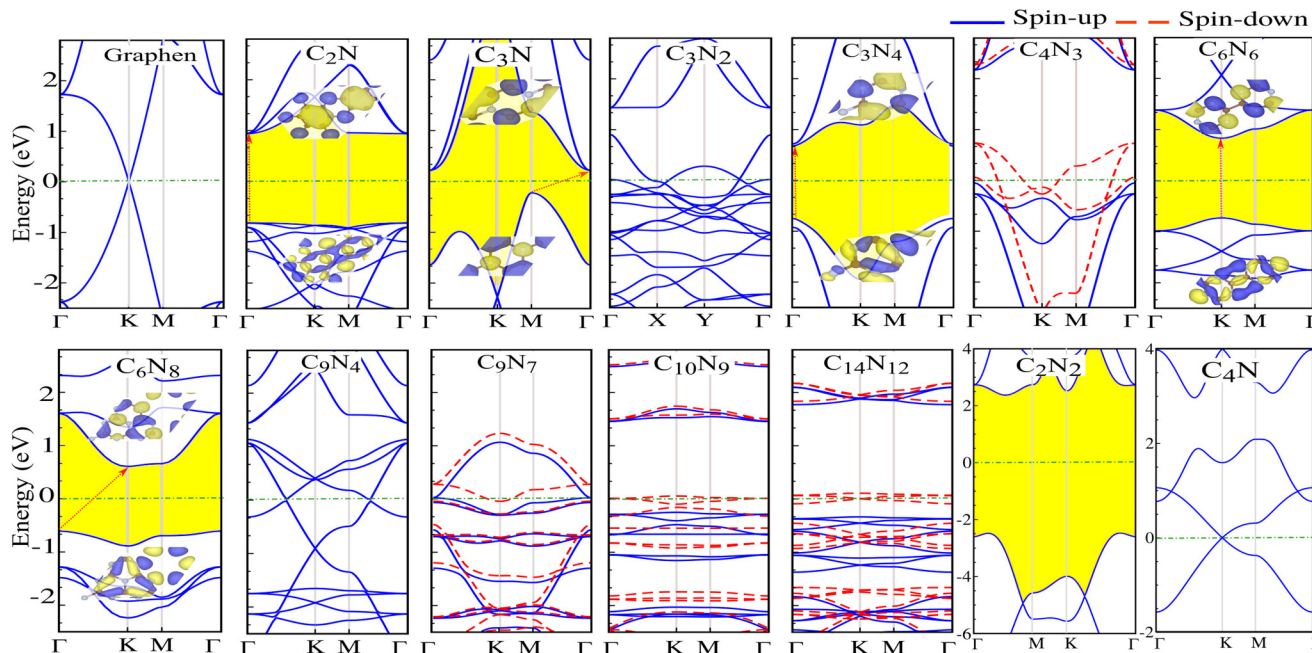

FIG. 2. Electronic band structure of graphene and 2DCN nanosheets. The insets are charge densities of minimum conduction band and the maximum valence band. The blue and yellow regions represent charge accumulation and depletion, respectively. The gap region between conduction and valence bands is colored yellow. The zero of energy is set to the Fermi level energy (E_F).

charge density, we found that the positively charged C atoms are surrounded by negatively charged N atoms. The total charge density shows a high charge density around the N atoms. This is in accordance with the Pauling scale electronegativity that N atoms have a larger electronegativity (C is 2.55 and N is 3.04), and thereby a large difference of electron density. Simulated STM images of graphene and 2DCN nanosheets are shown in Fig. S3 (see the supplementary material). The inset structure represents repeating unit cells, with the brown (blue) atoms representing C(N) atom. From the predicted STM images of 2DCN, it is easy to recognize and correlate them with the corresponding atomistic structure.

The electronic band structure of graphene and 2DCN nanosheets is shown in Fig. 2. It is well known that graphene is a semimetal with a zero gap at E_F where the valence and conduction bands cross with linear dispersions, so-called Dirac-cones in good agreement with Refs. 86–89. We see that C_2N is a direct semiconductor with a 1.75 eV bandgap, and the VBM and CBM are located at the Γ point. However, C_3N is a semiconductor with an indirect bandgap of 0.4 eV, where the VBM and CBM are located at Γ and M points, respectively. Our result is in agreement with previous

calculations.[10,90–93] A Dirac-point which is 2.25 eV below E_F is shown in the band structure of C_3N (see Fig. 2). The electronic structure of C_3N_2 exhibits a semimetal character, and we see three Dirac-points at and near E_F. There are two extra crossing points that are located along Γ-X and X-Y. This unique electronic property is different from other 2DCN, and this result coincides well with those obtained by previous calculations.[72,73] C_3N_4 is a direct semiconductor and has a 1.45 eV bandgap at the Γ point, which is in agreement with previous studies.[21,22] In contrast with C_3N_4, C_4N_3 is a half-metal with a 0.55 eV direct bandgap in the ↑ spin channel. In addition, the degeneracy of ↑ and ↓ spin channels is broken and shows spin-polarization at the E_F with $1\mu_B$ magnetic moment per unit cell. Our result is in agreement with previous calculations.[24–27,94] The band structure indicates that C_6N_6 is a wide bandgap semiconductor with gap values of 1.5, 2.4, and 1.35 eV that are located at the K, Γ, and M points, respectively (see Fig. 2). This result agrees with the previous report.[30]

C_6N_8 is an indirect semiconductor with a bandgap of 1.22 eV that agrees with Ref. 95. Similar to C_3N_2, C_9N_4 is a semimetal and we see that there are three Dirac-points at and near the E_F. At the
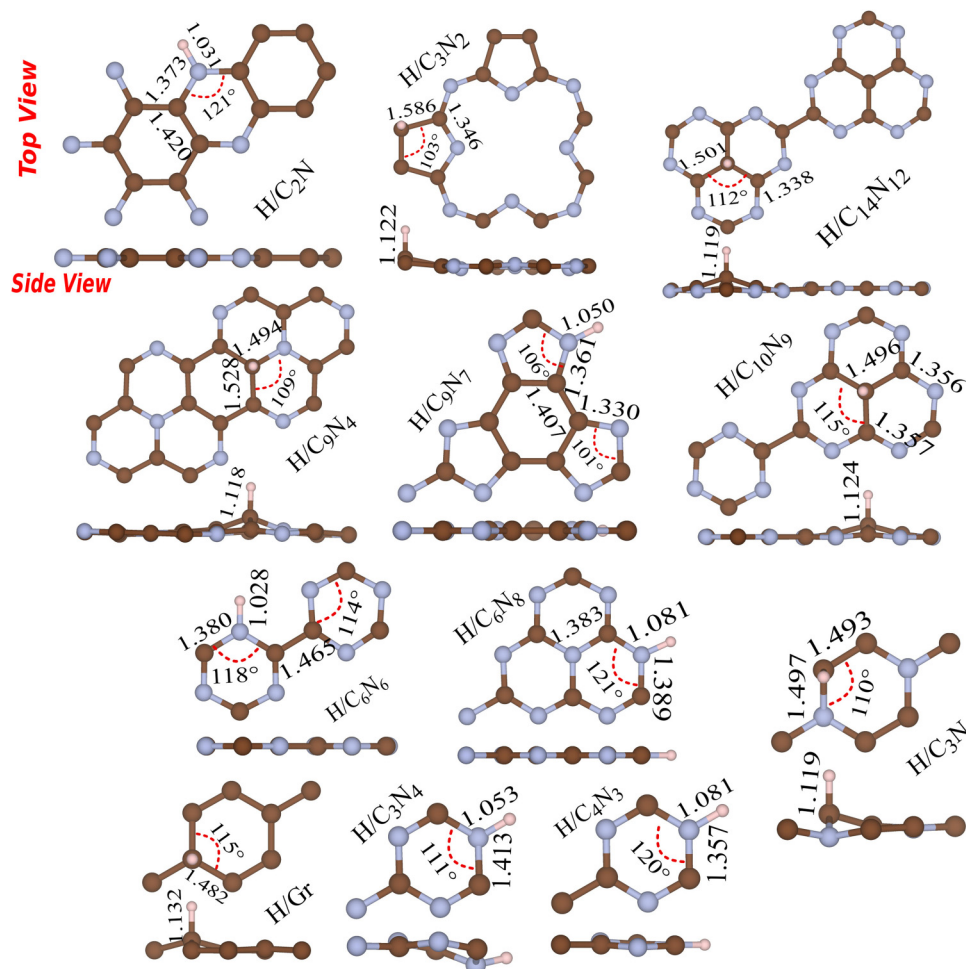

FIG. 3. Optimized structures of H adsorbed on graphene and 2DCN nanosheets with their structural properties. Top and side views are presented.
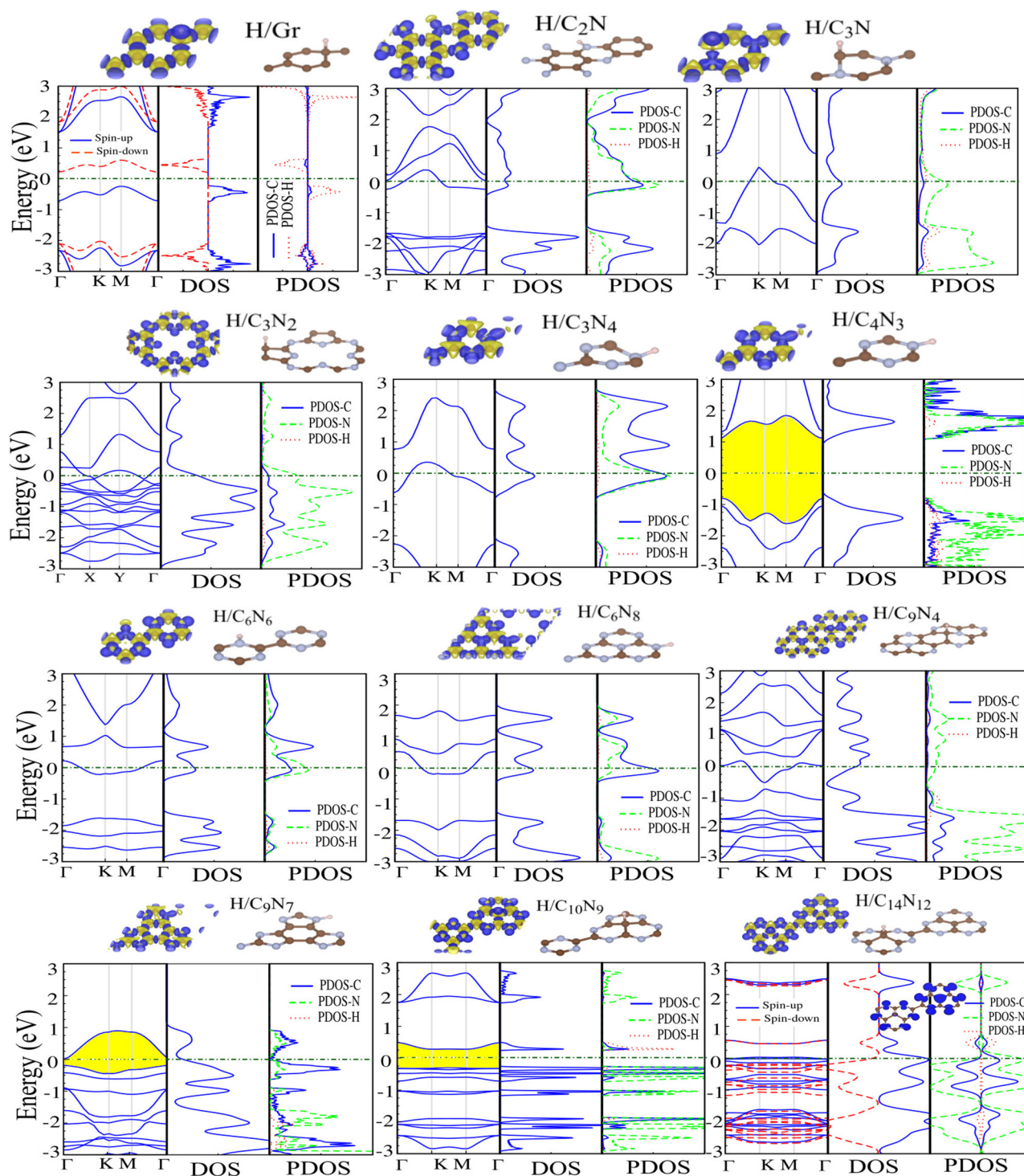
FIG. 4. Electronic band structure with the corresponding DOS of H-adsorbed graphene and 2DCN nanosheets. The difference charge density and optimized structures are shown in the same panel. The blue and yellow regions represent the charge accumulation and depletion, respectively. The difference spin density with magnetic moment is shown as the inset. The blue and yellow regions represent the ↑ and ↓ spin states, respectively. The zero of energy is set at E_F indicated by green dashed-dotted lines. The gap region between conduction and valence bands is colored yellow.

K point, there is one extra crossing point that is located $\sim 1\,eV$ below E_F and a narrow bandgap of 40 meV is seen near E_F, which agrees well with those obtained by a previous study.[81] For C_9N_7, the energy band splits into ↑ and ↓ spin channels resulting in a ferromagnetic-metal. It is interesting to see that C_9N_7 has a spin-polarized ground state with $0.8\mu_B$ magnetic moment per unit cell. Our result agrees well with Ref. 82. The band structures of $C_{10}N_9$ and $C_{14}N_{12}$ are shown in Fig. 2. We found that a remarkable spin-splitting occurs in the ↑ and ↓ spin channels near to E_F. The CB and VB of the ↓ spin channel meet in a single point at E_F, whereas bandgaps of approximately 1.7 eV ($C_{10}N_9$) and 2.1 eV ($C_{14}N_{12}$) are noted in the ↑ spin channel, exhibiting clear features of a spin-glass semiconductor. $C_{10}N_9$ and $C_{14}N_{12}$ have 1 and $2\mu_B$ magnetic moment in their ground states, respectively. Interestingly, the charge carriers (electrons and holes) near E_F behave differently around the meeting point. For $C_{10}N_9$, the VB and CB in the ↓ spin channel meet at the Γ point with parabolic energy-momentum dispersion relations, while for $C_{14}N_{12}$ two bands meet at the K point and have a linear energy dispersion characterized by the so-called Dirac-cones. The Dirac-cones in $C_{14}N_{12}$ are spin-polarized and energy bands split into ↑ and ↓ spin channels, which is different from graphene, C_3N_2, C_9N_4, and other Dirac materials. For C_4N, we see that the VBM and CBM energy bands touch each other at E_F and a Dirac-point is formed at E_F, implying a semimetallic character, like graphene. While C_2N_2 is an insulator with a 5 eV bandgap and interestingly we see two Dirac-points that are located $\sim 5\,eV$ below E_F. DOS and PDOS of pristine graphene and 2DCN nanosheets are shown in Fig. S4 (see the supplementary material). Direct semiconducting behavior of C_2N, C_3N, C_3N_4, C_6N_6, and C_6N_8 can be quite useful for nanoelectronic and optoelectronic applications. Note that the half-metallicity of C_4N_3 and the ferromagnetic behavior of C_9N_7 can be quite important for spintronic applications. The unusual semimetallic electronic property of C_4N, C_3N_2, and C_9N_4 shows Dirac-points at E_F, which can be important for various applications. The spin-gapless semiconductors $C_{10}N_9$ and $C_{14}N_{12}$ are expected to open up many prospects for practical applications, such as spin photodiodes, spin detectors, and electromagnetic radiation generators over a wide range of wavelengths based on spin photoconductivity.

IV. ADSORPTION OF H ATOM

Additionally, the adsorption of adatoms will affect the structural, electronic, and magnetic properties of pristine 2DCN nanosheets. The calculations are performed using a 2×2 supercell of C_3N, with fully structural optimizations, where all atoms are relaxed in all directions. The optimized atomic structures of a 2×2 supercell of graphene and 2DCN nanosheets are shown in Fig. S5 (a) of the supplementary material. Also, the variations of structural parameters including lattice constant, atomic bond lengths, and nanopore diameter, are shown in Figs. S5(b)–S5(d) of the supplementary material. After structural optimization of the 2×2 supercell of the 2DCN, we investigate the electronic and magnetic properties. The spin-polarized electronic band structure of the 2×2 supercell of graphene and different 2DCN is shown in Fig. S6 of the supplementary material.

Here, we consider the functionalization by hydrogen. The minimum energy or most stable sites of the H adatom on the
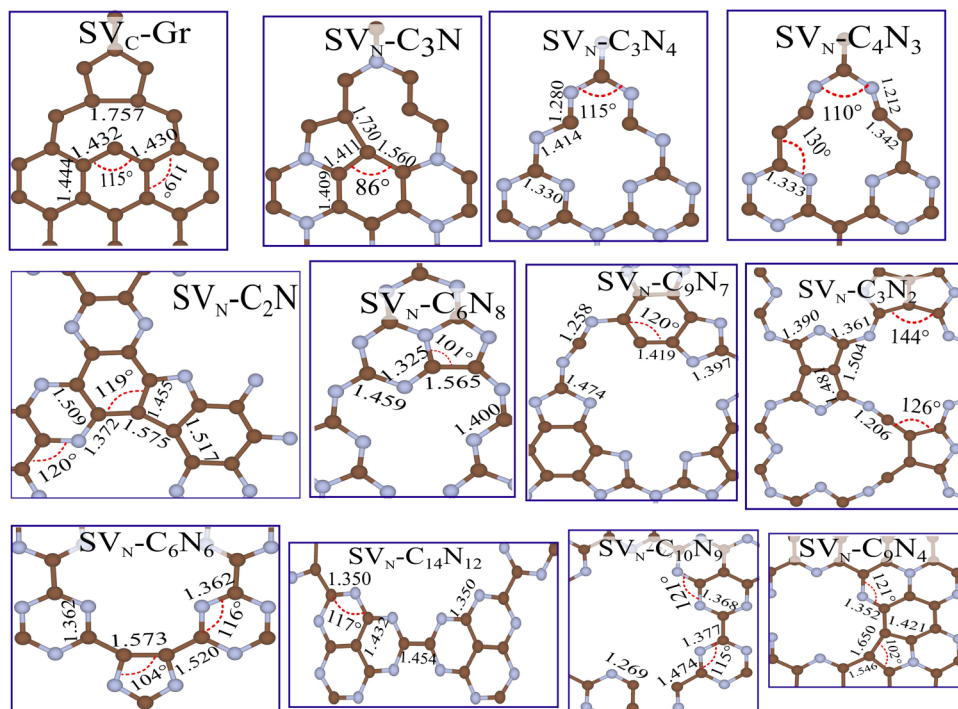

FIG. 5. Optimized structures of the N-vacant site of different 2DCN nanosheets and of the C-vacant site in graphene. Structural parameters including atomic bond length and bond angles are indicated. C, N, and H atoms are shown by brown, blue, and white colors, respectively.

surface of 2DCN are obtained by placing H on various preferable adsorption sites. With fully structure optimization, where all atoms are relaxed in all directions, we determine the most stable site as the minimum energy configuration among the different sites. In the following, when a H atom is adsorbed on a 2DCN nanosheet, we will label it as H/2DCN. The top and side views of optimized structures of H adsorbed on graphene and 2DCN nanosheets are shown in Fig. 3. The H atom is located right above a C atom of the C_3N and C_3N_2, forming a single covalent bond and a local distortion can occur in the structure and the C atoms directly below H undergoes a notable shifting toward the opposite direction, resulting in a buckling of about 0.5 Å. After relaxation, the C—H bond length is 1.12 Å, while the C—C and C—N bonds are elongated to 1.5 and 1.58 Å, respectively, which compares to the C—C bond length 1.42 Å in pristine nanosheets, while bond angles between C—C—C and C—N—C are in the range of 110° and 103°, respec-

tively, and show sp^3-hybridization character. For the C_3N_4, C_4N_3, C_6N_6, and C_6N_8 nanosheets, the H atom is bonded to the N atom and forms a covalent bond which results in elongated N—C bonds with lengths 1.35–141 Å, while the N—H bond lengths are very short in the range of 1.02–1.08 Å. For C_9N_4, $C_{10}N_9$, and $C_{14}N_{12}$ nanosheets, the H atom is located right above a C atom and a local deformation occurs around the H atom, and after relaxation, different C—H bond lengths are determined to be about 1.11–1.12 Å. We see that the C atoms directly below H move in the opposite direction, with 0.5 Å buckling of the plane.

The electronic band structure with corresponding DOS of H adsorbed graphene and 2DCN nanosheets is shown in Fig. 4. The difference charge density and optimized structures are shown in the same panel. For the H/Gr, there is a band spin-splitting around E_F
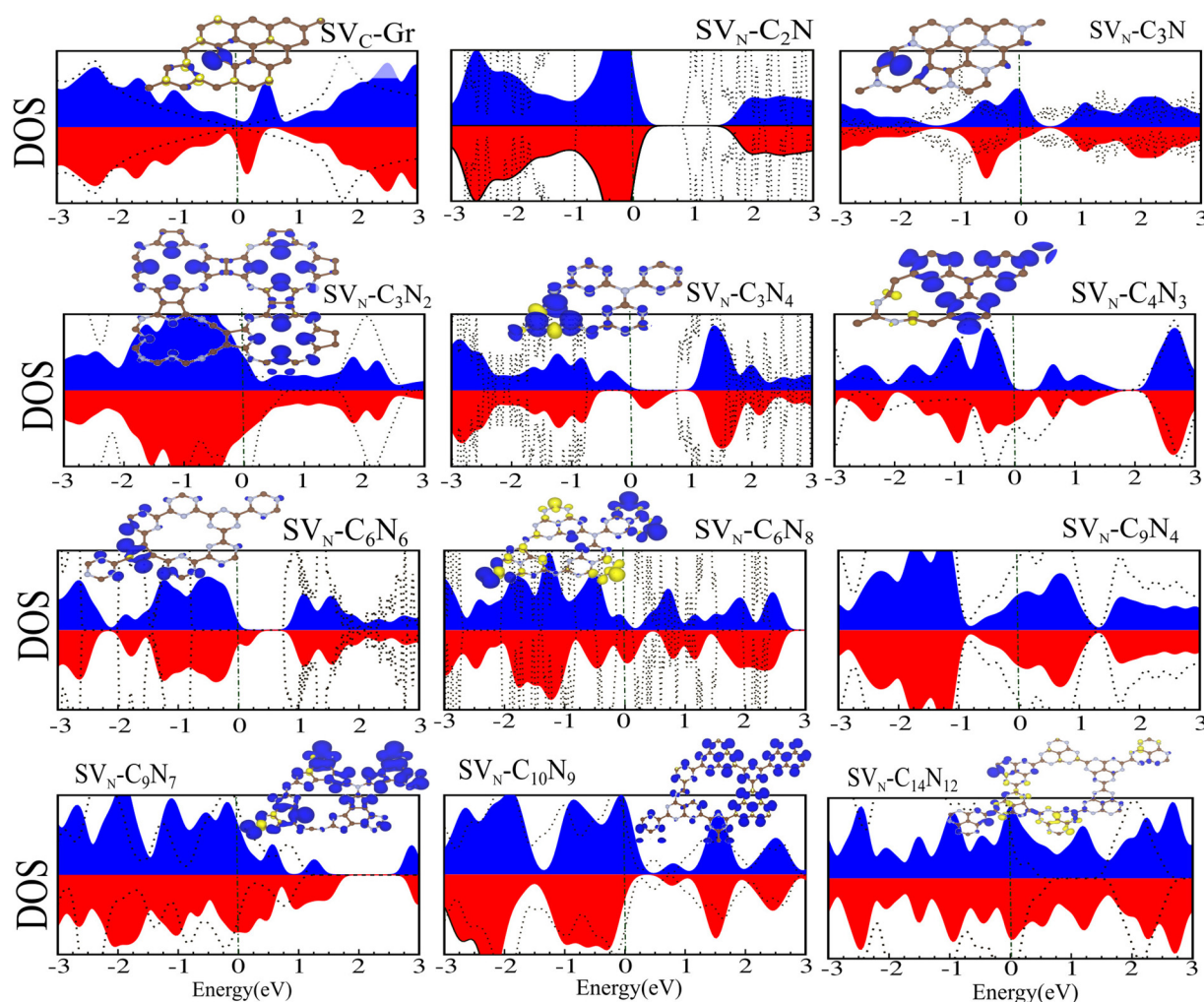

FIG. 6. Spin resolved DOS of the N-vacant site of different 2DCN nanosheets and for the C-vacant site of graphene. The difference spin density are shown as the insets. The blue and yellow regions represent the ↑ and ↓ spin states, respectively. The zero of energy is at E_F indicated by the green dashed-dotted vertical lines.
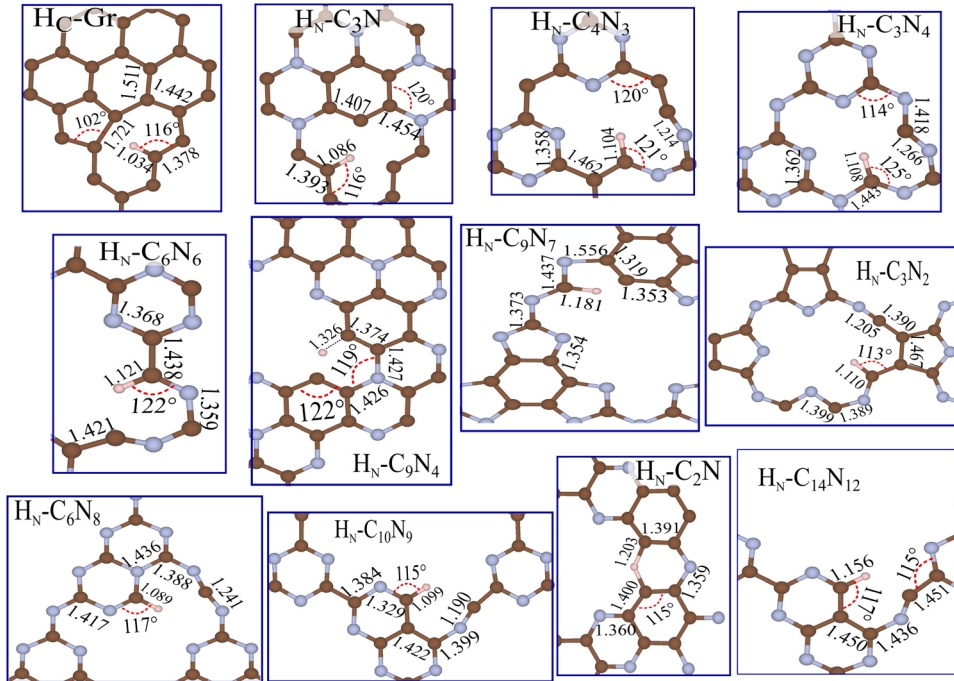
FIG. 7. Top view of optimized structures of H-substituted in the N-vacant site. The corresponding structural parameters including atomic bond length and bond angles are indicated. C, N, and H atoms are shown by brown, blue, and white colors, respectively.

into ↑ and ↓ spin channels. Thus, the system becomes a dilute-magnetic semiconductor with $1\mu_B$ magnetic moment. The Dirac-point disappears in H/Gr due to the strong disturbance of the p_z states caused by the adsorption of H atom.[96,97] The electronic structure of adsorbed H on C_2N, C_3N, and C_3N_2 is strongly modified. The energy bands below and above E_F are mainly originating from the H orbital states and appear as localized impurity states. H/C_2N, H/C_3N, and H/C_3N_2 are metals. From the PDOS of H/C_2N, we found that the electron states near E_F are mainly built up of C/N-p orbitals, while in H/C_3N and H/C_3N_2, they are due to the hybridization of C-p and N-p orbitals of the nearest atoms. The DOS of ↑ and ↓ spin states completely compensate each other and, therefore, the materials are nonmagnetic. The interaction of H atoms with C_3N_4, C_6N_6, and C_6N_8 eliminates the semiconducting behavior of the pristine system and become metals. C_4N_3 is a half-metal with $1\mu_B$ magnetic moment, while H/C_4N_3 becomes a direct semiconductor with a 2.0 eV bandgap. Based on the calculated PDOS, both the CBM and VBM receive contributions mainly from the hybridization of the C/N-p orbitals. H/C_9N_4 becomes a metal, and the Dirac-point vanishes due to H adsorption. C_9N_7 becomes a ferromagnetic-metal and has $1\mu_B$ magnetic moment, while H/C_4N_3 is an indirect semiconductor with a 0.2 eV bandgap and both ↑ and ↓ spin bands overlap, with no net spin polarization. The interaction of H with $C_{10}N_9$ eliminates the spin-glass semiconducting character and turns it into a direct semiconductor with a 0.6 eV bandgap. Interestingly, the ↑ and ↓ spin channels for $H/C_{14}N_{12}$ exhibit half-metal behaviors and induce $1\mu_B$ magnetic moment in the ground state. As can be seen from DOS and PDOS, for H/C_9N_4, the electron states near E_F are mainly governed by the N-p orbitals, while for $H/C_{14}N_{12}$, the VBM and CBM are due to

the hybridization of C-p and N-p orbitals. In H/C_9N_4, the VBM and CBM are due to the hybridization of C/N-p and H-s with N-p orbitals, respectively. To illustrate the bond character more in detail, the difference charge density is shown as the insets in Fig. 4. We note there is charge accumulation in the region between H and the neighboring C and N atoms, resulting in a strong covalent bond of the H–C and H–N bonds. For clarity of the spin arrangement on each atom and to further elucidate the origin of magnetism, difference spin density is shown as the insets in Fig. 4.

V. N-VACANCY

Here, we will study the effect of N-vacancy defects. We remove one N atom at every hexagonal and in this way produce a single vacancy of N atom (SV_N). The defective structures are fully relaxed and the total energies and band structures are calculated. The top and side views of optimized atomic structures as well as their bond lengths and bond angles of the N-vacant site of various 2DCN, are shown in Fig. 5. The C and N atoms around the N-vacant site in C_2N, C_3N, C_3N_2, C_6N_6, C_9N_4, and $C_{14}N_{12}$ undergo a Jahn-Teller distortion,[98] and C atoms close to the vacancy site move toward each other to form C–C bonds. For these structures, Jahn-Teller distortion creates a five-membered ring via an elongated bond between two of the C atoms nearest to the vacancy. We found for the C–C and N–C bond lengths, respectively, 1.50 and 1.75 Å (see Fig. 5). For some of the other 2DCN after relaxation of the structure, the structural distortion that stems from the N vacancy cannot be compensated by the local reconstruction of neighboring C atoms. No covalent bond at the N-vacant site is found but the C and N bond lengths around the

N-vacant site are modified. All 2DCN stay completely planar. The band structure of the N-vacant site of 2DCN nanosheets is shown in Fig. S7 of the supplementary material. Our result shows that graphene with a C-vacancy, induce defect states around E_F, resulting

in a half-metallic behavior and inducing a $1\mu_B$ magnetic moment. We can see that C_3N, C_3N_2, C_9N_7, and $C_{14}N_{12}$ with a N-vacancy are ferromagnetic-metal. C_2N and C_9N_4 with a N-vacancy, defect states appear around E_F and induce metallic properties. With a
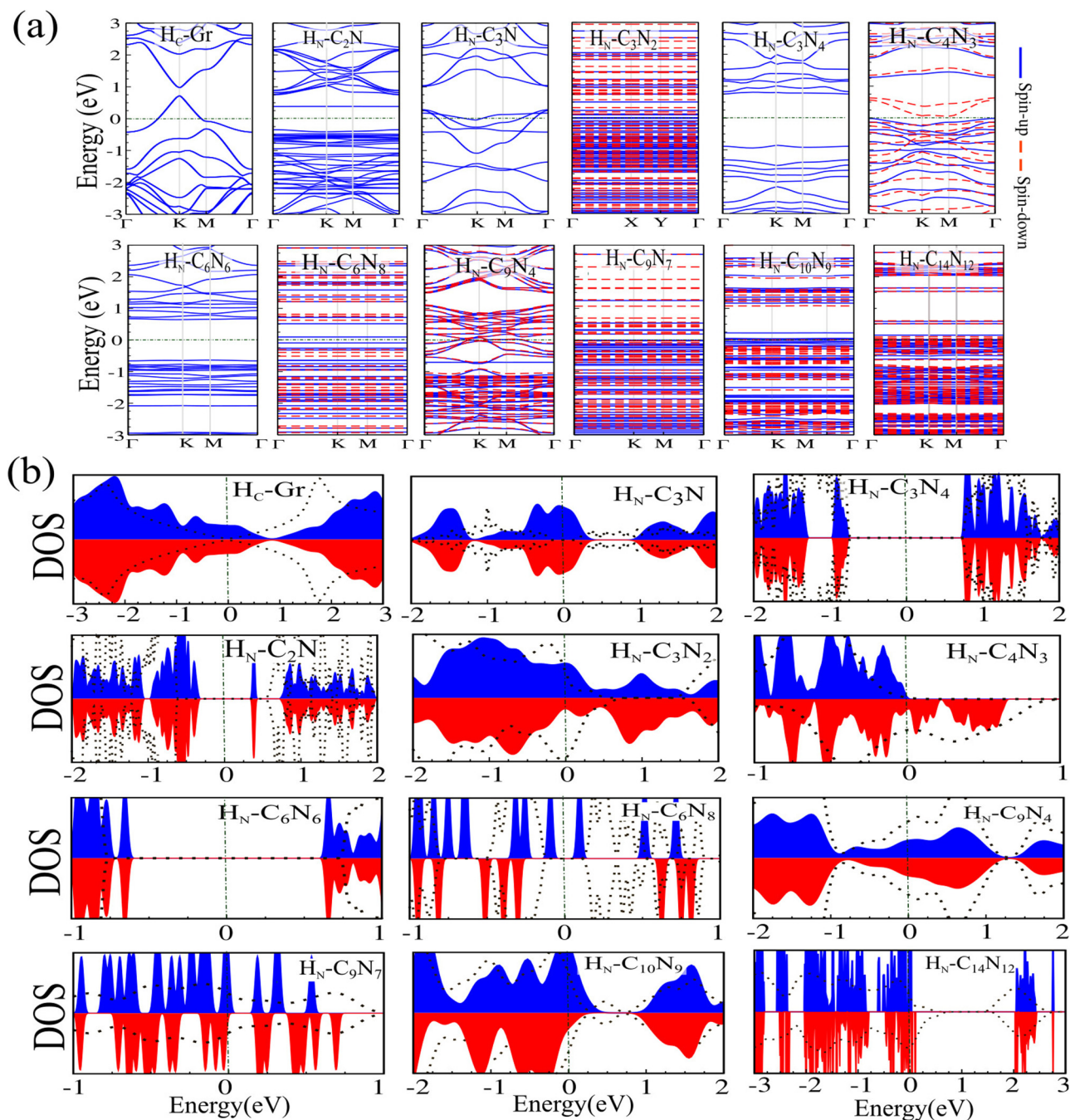

FIG. 8. (a) Electronic structure and (b) DOS of H-substituted in the N-vacant site. The zero of energy is set at the E_F indicated by green dashed-dotted lines.
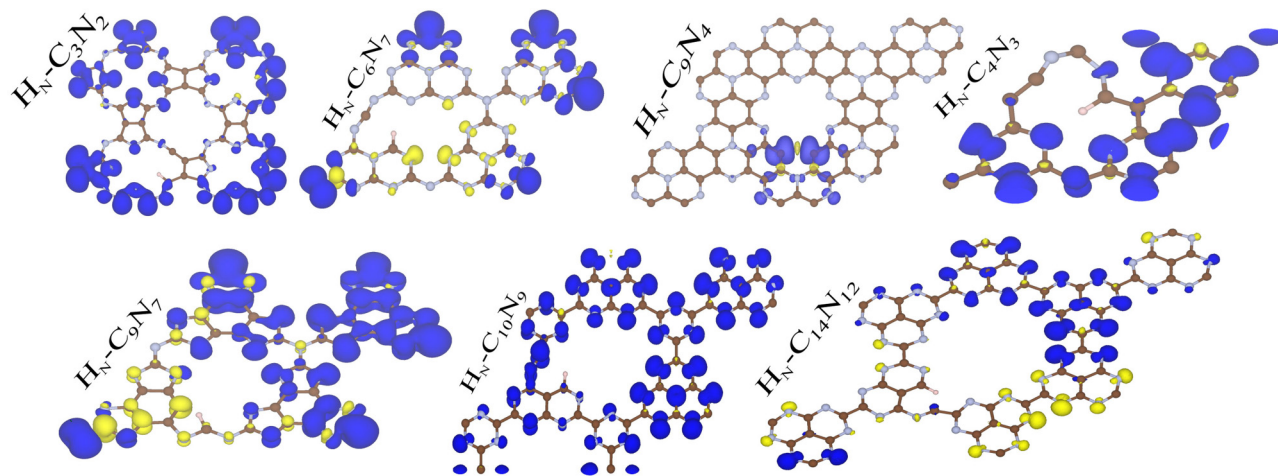
FIG. 9. Difference spin density of H-substituted in the N-vacant site of 2DCN nanosheets. The blue and yellow regions represent the ↑ and ↓ spin states, respectively.

N-vacancy, C_4N_3 becomes a spin-glass semiconductor, while C_3N_4, C_6N_6, and $C_6N_8, C_{10}N_9$ are dilute-magnetic semiconductors (see Fig. 6). The magnetic moments of dilute-magnetic semiconductor and ferromagnetic-metal structures with the N-vacancy are in the range of 0.3 (C_3N)–7.5 $(C_9N_7)\mu_B$. The spin resolved DOS of the

N-vacant site of different 2DCN nanosheets and for the C-vacant site of graphene is shown in Fig. 6. The difference spin density is shown as the insets. It is also seen from the DOS that the density of N-vacant site is very high and the state at E_F of a N-vacancy belongs to the C/N-p orbital around the missing N atom. The
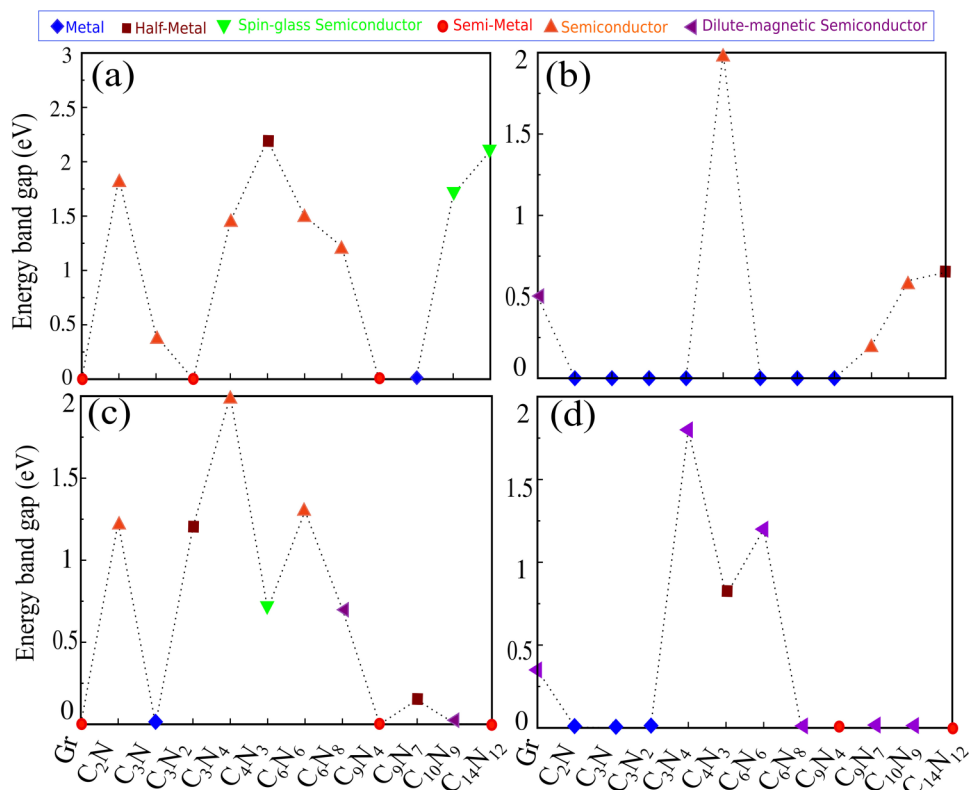

FIG. 10. Variation of bandgap of (a) 2DCN, (b) H-adsorbed 2DCN, (c) H-substituted 2DCN, and (d) N-vacancy 2DCN.

energy band of 2DCN is strongly disturbed by the N-vacant site, thus the bonding between atoms should be a covalent bond. To illustrate the bond character more clearly, the differential charge density for 2DCN with th N-vacant site is presented in Fig. S8 of the supplementary material. There is a charge accumulation in the region around SV_N that leads to a strong covalent bond character of the C and N bonds. Our results show that the N-vacant site in 2DCN can modify the electronic structure and tune the bandgap and magnetism in these structures. Our result shows that graphene with a C-vacancy induces defect states around E_F, resulting in a half-metallic behavior and inducing a $1\mu_B$ magnetic moment. We see that C_3N, C_3N_2, C_9N_7, and $C_{14}N_{12}$ with a N-vacancy are ferromagnetic-metal. C_2N and C_9N_4 with a N-vacancy defect states appear around E_F and induce metallic properties.

VI. SUBSTITUTION OF N BY H

In the experimental synthesis of nanomaterials, the N-vacant sites are more likely to be substituted by an H atom. Therefore, we consider N substitution by H which we label as H_N-C2DCN. Calculations are performed using a 2×2 supercell of 2DCN, with fully structure optimizations, where all atoms are relaxed in all directions. The top view of optimized structures of H-substituted in the N-vacant site is shown in Fig. 7. The corresponding, structural parameters including atomic bond length and bond angles are indicated. C, N, and H atoms are shown by brown, blue, and white

colors, respectively. The H_N-2DCN shows a local distortion that is minute and the hexagonal crystal symmetry of 2DCN is not strongly modified. The H atom interacts through sp^2-hybridization and forms one σ bond with the nearest C atom of the different 2DCN. The C—H bond lengths of 2DCN are in the range of $\sim$1.08–1.12 Å, which are small, indicating a strong interaction between the H and C atoms. We note that the bond length of C—C and N—C atoms and bond angles around H_N are modified. H_N in C_2N, C_3N_4, C_4N_3, and C_6N_6 changes the bond lengths and bond angle, and corrugation of the planar structures is found. For the other 2DCN nanosheets with H_N, there is only a minute effect on the planar structure. The electronic structure and DOS of H-substituted in the N-vacant site are shown in Figs. 8(a) and 8(b). Defect states appear near E_F, induce metallic character, and the system turns to a nonmagnetic metal. $H_N C_4 N_3$ becomes a spin-glass semiconductor and induce $2\mu_B$ magnetic moment. While C_2N, C_3N_4, C_6N_6 with H_N are semiconductors. Difference spin density of the H-substituted N-vacant site of 2DCN nanosheets is shown in Fig. 9. The blue and yellow regions represent the ↑ and ↓ spin states, respectively. The differential charge density is presented in Fig. S9 of the supplementary material. The blue and yellow regions represent charge accumulation and depletion, respectively. We can see an obvious charge accumulation in the region around H_N resulting in a strong covalent bond of the C and N bonds. The variations of the bandgap and the magnetic moment of 2DCN, H-adsorbed 2DCN, H-substituted 2DCN and N-vacancy 2DCN
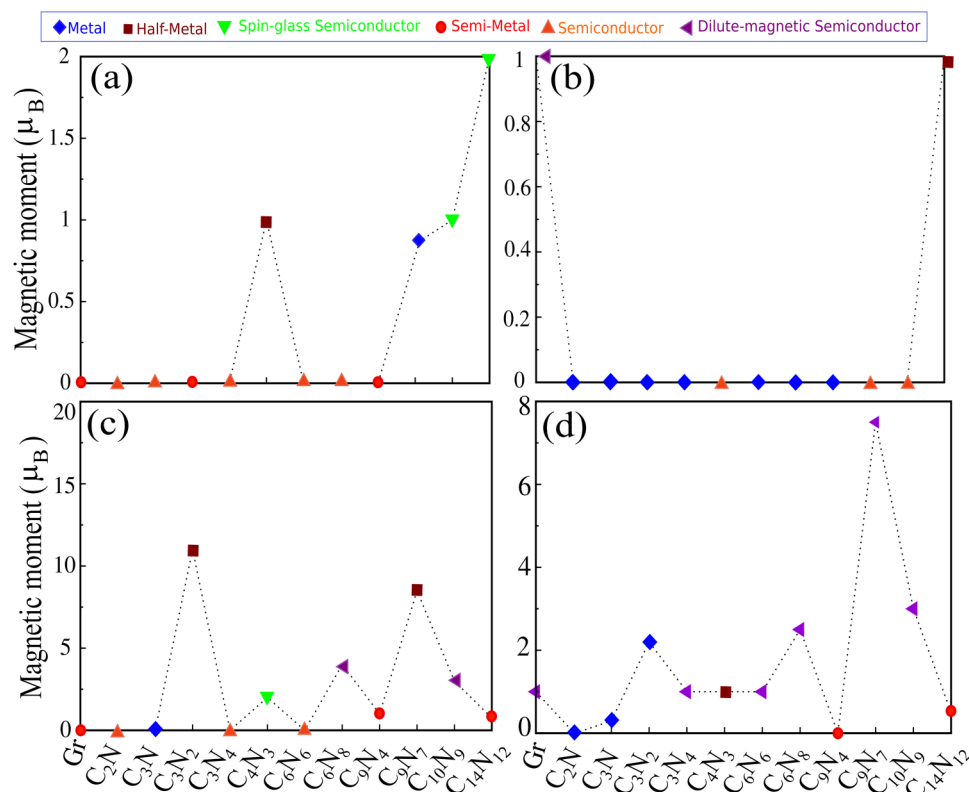

FIG. 11. Variation of magnetic moment of (a) 2DCN, (b) H-adsorbed 2DCN, (c) H-substituted 2DCN, and (d) N-vacancy 2DCN.

are shown in Figs. 10(a)–10(d) and Figs. 11(a)–11(d). Our result shows that the electronic structure of pristine 2DCN nanosheets is modified and exhibits a diversity of electronic properties including metal, semimetal, half-metal, ferromagnetic-metal, semiconductor, spin-glass semiconductor, and insulator.

VII. SUBSTITUTION OF N BY C

The electronic band structures with the corresponding DOS and PDOS of N substituted by C in different 2DCN nanosheets are shown in Figs. 12 and 13. The optimized atomic structures and difference charge densities are shown as the insets. The substitution of N with C modifies the electronic structure and gives rise to localized states in the energy bandgap. The C-substituted C_3N_2, C_3N_4, C_4N_3, and C_9N_7 exhibit the ferromagnetic-metal character, and spin-splitting occurs in the ↑ and ↓ spin channels and induce, respectively, 0.2, 0.6, 0.5, and $1.3\mu_B$ magnetic moments in the ground state. From PDOS, we see that the metallic state is generated by the hybridization of the N/C-p_z (C_3N_2), N/C-$p_{x,y}$ (C_3N_4, C_4N_3), and N/C-s, $p_{x,y,z}$ (C_9N_7) orbitals, while C-substituted C_3N and C_4N becomes a metal because we observe a band crossing at E_F. Both ↑ and ↓ spin bands overlap, and thus there is no spin-polarized state. From the calculated PDOS, we see that the impurity

states are mainly from the hybridization of the N/C-p_z orbitals. For the C-substituted C_2N, C_6N_6, and C_6N_8, the degeneracy of both the ↑ and ↓ spin channels is broken and become a dilute-magnetic semiconductor with $1\mu_B$ magnetic moment. The direct bandgap of C_N-C_2N is 1.6 eV, while the VBM and CBM are located at the Γ point. For the C-C_2N, the VBM mainly originates from the hybridization of C/N-s, $p_{x,y}$, while the CBM comes from C/N-s, p_z in ↑ spin channel. While the C_N-C_6N_6 (C_N-C_6N_8), have a direct (indirect) bandgap of 1.5 eV (1.3 eV) and an indirect gap of 1.8 eV (direct 1.3 eV) in the ↑ and ↓ spin channels, respectively. The VBM of C_6N_8 mainly originates from C/N-$p_{x,y}$ in ↑ spin channel, while the CBM originates from C-s, $p_{x,y}$ in the ↓ spin channel. C_N-C_9N_4, is a dilute-magnetic semiconductor and induce $1\mu_B$ magnetic moment. A nontrivial direct bandgap of 70 and 100 meV in the ↑ spin channel, while the VBM and CBM are located between Γ-K points. We see in the ↓ spin channel, 30 meV and 50 meV nontrivial indirect bandgap and the VBM and CBM are located at the K and Γ points, respectively. C_N-$C_{10}N_9$, becomes a direct semiconductor with a 0.7 eV bandgap and the VBM mainly originates from the hybridization of C-p_z with the C/N-$p_{x,y,z}$ orbital, while the CBM is built from C-$p_{x,y,z}$.

C_N-$C_{14}N_{12}$ turns into a spin-glass semiconductor with $1\mu_B$ magnetic moment. The ↑ spin channel is a direct semiconductor
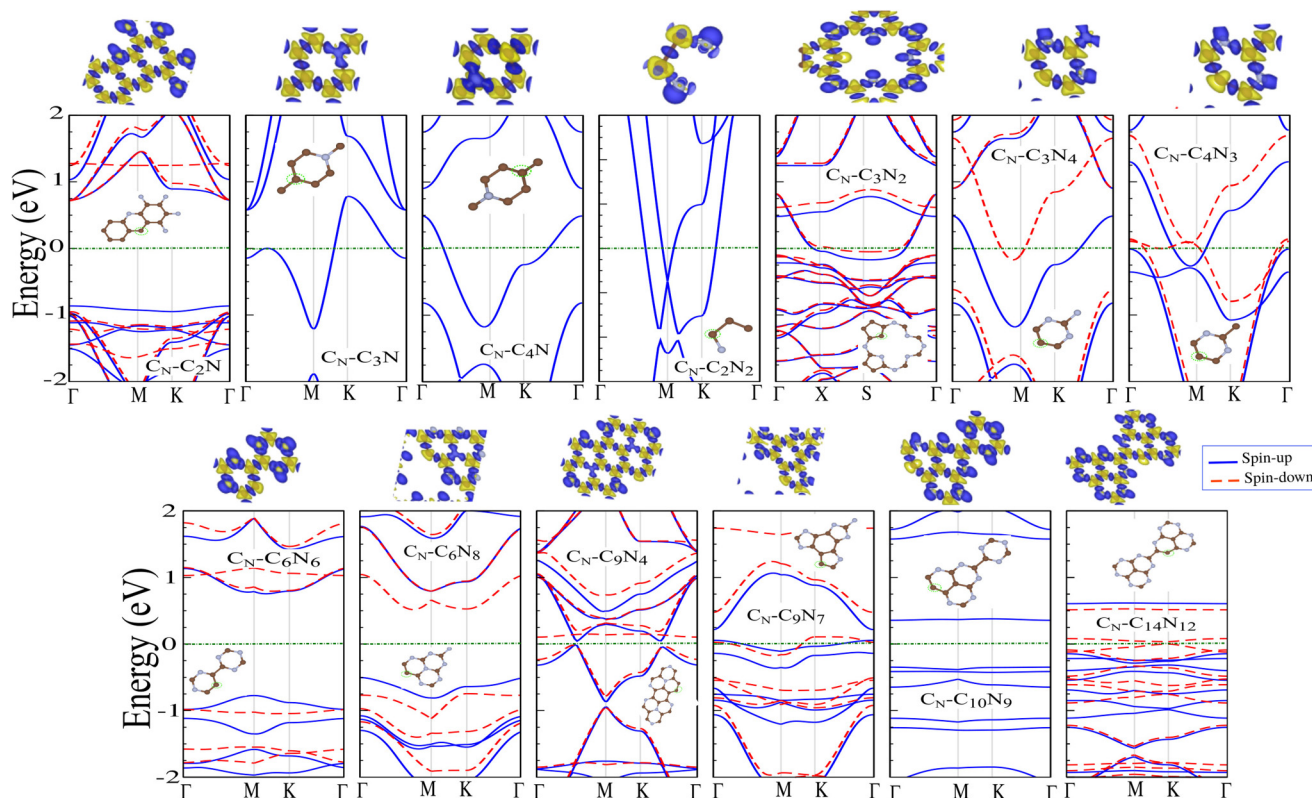

FIG. 12. Electronic band structure of C-substituted 2DCN nanosheets. The insets are the top view of the optimized structures and difference charge densities. The blue and yellow regions represent the charge accumulation and depletion, respectively. The zero of energy is set at the E_F indicated by green dashed-dotted lines.
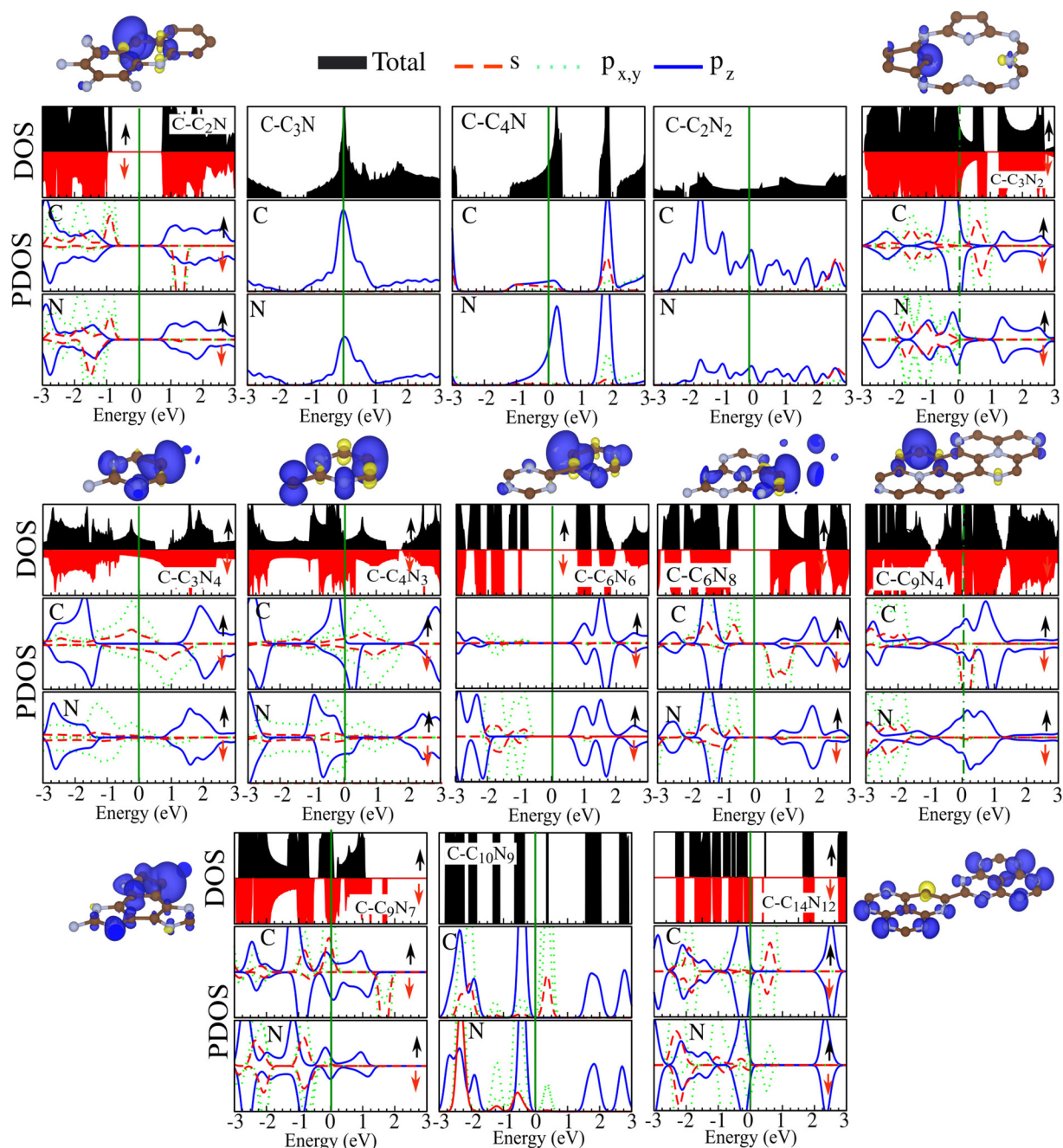
FIG. 13. DOS and PDOS of C-substituted 2DCN nanosheets. The difference spin density is shown in the insets. The blue and yellow regions represent the ↑ and ↓ spin directions, respectively. The zero of energy is set at E_F indicated by green dashed-dotted vertical lines.

with a 0.8 eV bandgap, while in the ↓ spin channel, the Dirac-point is eliminated and there is the opening of a 40 meV nontrivial bandgap at E_F. The VBM mainly originates from the hybridization of C/N-$p_{x,y,z}$, while the CBM comes from C-$p_{x,y}$ at the ↑ spin

channel. We see that the optimized structures of C-substituted 2DCN do not have any local deformation. The difference charge density is shown in Fig. 12 as insets. We note there is a charge accumulation in the region between C-substituted atoms and the

neighboring atoms, giving a strongly covalent bond character in the formed substituted C—C or C—N bonds. To further clearly understand the magnetic states of the doped systems, the difference spin density is plotted in Fig. 13. The blue and yellow regions represent the ↑ and ↓ spin states, respectively. The order of magnetic coupling in C_3N_4 and C_9N_7 is ferromagnetic, while the other magnetic structures exhibit antiferromagnetic interaction. The magnetic moment results from the C atom and partly from the neighbor C and N atoms, and the spin density is entirely localized at the C-substituted impurity.

VIII. CONCLUSION

Two-dimensional carbon-nitride (2DCN) nanomaterials have emerged recently as a prominent member of nanomaterials beyond graphene. In summary, by employing extensive first-principles calculations, we investigated the structural, electronic and magnetic properties of 2DCN nanosheets of already synthesized (C_2N, C_3N, C_3N_4, C_4N_3, C_6N_6, and C_6N_8) as well as predict novel one (C_3N_2, C_9N_4, C_9N_7, $C_{10}N_9$, and $C_{14}N_{12}$). Energy-band structure calculations show that 2DCN gives rise to diverse electronic properties including semimetal (C_3N_2, C_4N, and C_9N_4), half-metal (C_4N_3), ferromagnetic-metal (C_9N_7), semiconductor (C_2N, C_3N, C_3N_4, C_6N_6, and C_6N_8), spin-glass semiconductor ($C_{10}N_9$ and $C_{14}N_{12}$), and insulator (C_2N_2). We showed how point defects of vacancies, substitutions, and interstitial impurities modify the electronic properties. Furthermore, the effects due to adsorption and substitution of hydrogen atoms as well as N-vacancy defects are investigated. Our results show that, in doing so, the electronic and magnetic properties can be adjustable and allow to tune the bandgap and magnetism. Tunable magnetism and bandgap in 2DCN nanosheets is highly desirable for its use in nanoscale optoelectronic devices.

IX. SUPPLEMENTARY MATERIAL

See the supplementary material for the tuning of novel electronic and magnetic properties by hydrogenation, atom substitution, and defect engineering.

ACKNOWLEDGMENTS

REFERENCES

[1]J. Li, W. Cui, Y. Sun, Yi. Chu, W. Cen, and F. Dong, "Directional electron delivery via a vertical channel between g-C_3N_4 layers promotes photocatalytic efficiency," J. Mater. Chem. A **5**, 9358–9364 (2017).

[2]Y. Zheng, J. Liu, J. Liang, M. Jaroniec, and S. Z. Qiao, "Graphitic carbon nitride materials: Controllable synthesis and applications in fuel cells and photocatalysis," Energy Environ. Sci. **5**, 6717–6731 (2012).

[3]A. Thomas, A. Fischer, F. Goettmann, M. Antonietti, J.-O. Müller, R. Schlögl, and J. M. Carlsson, "Graphitic carbon nitride materials: Variation of structure and morphology and their use as metal-free catalysts," J. Mater. Chem. **18**, 4893 (2008).

[4]Y. Zheng, Y. Jiao, J. Chen, J. Liu, J. Liang, A. Du, W. Zhang, Z. Zhu, S. C. Smith, M. Jaroniec, G. Q. (Max) Lu, and S. Z. Qiao, "Nanoporous graphitic-C_3N_4 @carbon metal-free electrocatalysts for highly efficient oxygen reduction," J. Am. Chem. Soc. **133**, 20116–20119 (2011).

[5]S. M. Lyth, Y. Nabae, N. M. Islam, S. Kuroki, M. Kakimoto, and S. Miyata, "Electrochemical oxygen reduction activity of carbon nitride supported on carbon black," J. Electrochem. Soc. **158**, B194–B201 (2011).

[6]S. M. Lyth, Y. Nabae, S. Moriya, S. Kuroki, M. A. Kakimoto, J. I. Ozaki, and S. Miyata, "Carbon nitride as a nonprecious catalyst for electrochemical oxygen reduction," J. Phys. Chem. C **113**, 20148–20151 (2009).

[7]M. Makaremi, S. Grixti, K. T. Butler, G. A. Ozin, and C. V. Singh, "Band engineering of carbon nitride monolayers by N-type, P-type, and isoelectronic doping for photocatalytic applications," ACS Appl. Mater. Interfaces **10**, 11143–11151 (2018).

[8]A. Rajabpour, S. Bazrafshan, and S. Volz, "Carbon-nitride 2D nanostructures: Thermal conductivity and interfacial thermal conductance with the silica substrate," Phys. Chem. Chem. Phys. **21**, 2507–2512 (2019).

[9]M. Javeed, L. E. Kwang, J. Minbok, S. Dongbin, J. In-Yup, J. Sun-Min, C. Hyun-Jung, S. Jeong-Min, B. Seo-Yoon, S. So-Dam, P. Noejung, O. J. Hak, S. Hyung-Joon, and B. Jong-Beom, "Nitrogenated holey two-dimensional structures," Nat. Commun. **6**, 6486 (2015).

[10]J. Mahmood, E. K. Lee, M. Jung, D. Shin, H. J. Choi, J. M. Seo, S. M. Jung, D. Kim, F. Li, M. S. Lah, N. Park, H. J. Shin, J. H. Oh, and J. B. Baek, "Two-dimensional polyaniline (C_3N) from carbonized organic single crystals in solid state," Proc. Natl. Acad. Sci. U.S.A. **113**, 7414–7419 (2016).

[11]B. Mortazavi, O. Rahaman, T. Rabczuk, and L. F. C. Pereira, "Thermal conductivity and mechanical properties of nitrogenated holey graphene," Carbon **106**, 1–8 (2016).

[12]B. Mortazavi, "Ultra high stiffness and thermal conductivity of graphene like C_3N," Carbon **118**, 25–34 (2017).

[13]A. Bafekry, S. F. Shayesteh, and F. M. Peeters, "C_3N monolayer: Exploring the emerging of novel electronic and magnetic properties with adatom adsorption, functionalizations, electric field, charging and strain," J. Phys. Chem. C **123**, 12485–12499 (2019).

[14]M. Makaremi, B. Mortazavi, and C. V. Singh, "Adsorption of metallic, metalloidic, and nonmetallic adatoms on two-dimensional C_3N," Phys. Chem. C **121**, 18575–18583 (2017).

[15]A. Bafekry, M. Ghergherehchi, S. Farjami Shayesteh, and F. M. Peeters, "Adsorption of molecules on C_3N nanosheet: A first-principles calculations," Chem. Phys. **526**, 110442 (2019).

[16]M. B. Tagani, "Electrical and mechanical properties of a fully hydrogenated two-dimensional polyaniline sheet," Comput. Mater. Sci. **153**, 126–133 (2018).

[17]M. B. Tagani and S. I. Vishkayi, "Polyaniline (C_3N) nanoribbons: Magnetic metal, semiconductor, and half-metal," J. Appl. Phys. **124**, 084304 (2018).

[18]M. D. Esrafili and S. Heydari, "B-doped C_3N monolayer: A robust catalyst for oxidation of carbon monoxide," Theor. Chem. Acc. **138**, 57 (2019).

[19]M. D. Esrafili and S. Heydari, "Catalytic reduction of nitrous oxide over boron-doped C_3N monolayers: A DFT study," Chem. Phys. Lett. **725**, 52–58 (2019).

[20]O. Faye, T. Hussain, A. Karton, and J. Szpunar, "Tailoring the capability of carbon nitride (C_3N) nanosheets toward hydrogen storage upon light transition metal decoration," Nanotechnology **30**, 75404 (2018).

[21]Zh. Guizhi, L. Kun, S. Qiang, K. Yoshiyuki, and J. Puru, "Lithium-doped triazine-based graphitic C_3N_4 sheet for hydrogen storage at ambient temperature," Comput. Mater. Sci. **81**, 275–279 (2014).

[22]X. Li, S. Zhang, and Q. Wang, "Stability and physical properties of a tri-ring based porous g-C_4N_3 sheet," Phys. Chem. Chem. Phys. **15**, 7142–7146 (2013).

[23]A. J. Mannix, B. Kiraly, M. C. Hersam, and N. P. Guisinger, "Synthesis and chemistry of elemental 2D materials," Nat. Rev. Chem. **1**, 0014 (2017).

[24]A. Du, S. Sanvito, and S. C. Smith, "First-principles prediction of metal-free magnetism and intrinsic half-metallicity in graphitic carbon nitride," Phys. Rev. Lett. **108**, 197207 (2012).

[25]T. Hu, A. Hashmi, and J. Hong, "Transparent half metallic g-C_4N_3 nanotubes: Potential multifunctional applications for spintronics and optical devices," Sci. Rep. **4**, 6059 (2014).

[26] A. Hashmi and J. Hong, "Metal free half metallicity in 2D system: Structural and magnetic properties of g-C_4N_3 on BN," Sci. Rep. **4**, 4374 (2014).

[27] X. Zhang, M. Zhao, A. Wang, X. Wang, and A. Du, "Spin-polarization and ferromagnetism of graphitic carbon nitride materials," J. Mater. Chem. C **1**, 6265–6270 (2013).

[28] Q. Guo, Q. Yang, Ch. Yi, L. Zhu, and Y. Xie, "Synthesis of carbon nitrides with graphite-like or onion-like lamellar structures via a solvent-free route at low temperatures," Carbon **43**, 1386–1391 (2005).

[29] J. Li, C. Cao, J. Hao, H. Qiu, Y. Xu, and H. Zhu, "Self-assembled one-dimensional carbon nitride architectures," Diam. Relat. Mater. **15**, 1593–1600 (2006).

[30] H. Qiu, Z. Wang, and X. Sheng, "First-principles prediction of an intrinsic half-metallic graphitic hydrogenated carbon nitride," Phys. Lett. A **377**, 347–350 (2013).

[31] A. Wang, X. Zhang, and M. Zhao, "Topological insulator states in a honeycomb lattice of s-triazines," Nanoscale **6**, 11157–11162 (2014).

[32] V. Arkady, J. P. Rabe, U. Kaiser, A. I. Cooper, A. Thomas, M. J. Bojdys, G. Algara-Siller, N. Severin, S. Y. Chong, T. Björkman, R. G. Palgrave, A. Laybourn, M. Antonietti, Y. Z. Khimyak, and A. V. Krasheninnikov, "Triazine-based graphitic carbon nitride: A two-dimensional semiconductor," Angew. Chem. **126**, 7580–7585 (2014).

[33] C. Xu, G. Luo, Q. Liu, J. Zheng, Zh. Zhang, Sh. Nagase, Zh. Gao, and J. Lu, "Giant magnetoresistance in silicene nanoribbons," Nanoscale **4**, 3111–3117 (2012).

[34] Z. Ni, H. Zhong, X. Jiang, R. Quhe, G. Luo, Y. Wang, M. Ye, J. Yang, J. Shi, and J. Lu, "Tunable band gap and doping type in silicene by surface adsorption: Towards tunneling transistors," Nanoscale **6**, 7609–7618 (2014).

[35] F. Banhart, J. Kotakoski, and A. V. Krasheninnikov, "Structural defects in graphene," ACS Nano **5**, 26–41 (2011).

[36] X. Peng and R. Ahuja, "Symmetry breaking induced band gap in epitaxial graphene layers on SiC," Nano Lett. **8**, 4464–4468 (2008).

[37] J. Gao, J. Zhang, H. Liu, Q. Zhang, and J. Zhao, "Structures, mobilities, electronic and magnetic properties of point defects in silicene," Nanoscale **5**, 9785–9792 (2013).

[38] W. Hu and J. Yang, "Defects in phosphorene," Phys. Chem. C **119**, 20474–20480 (2015).

[39] W. Xiong, C. Xia, T. Wang, J. Du, Y. Peng, X. Zhao, and Y. Jia, "Tuning electronic structures of the stanene monolayer via defects and transition-metal-embedding: Spin-orbit coupling," Phys. Chem. Chem. Phys. **18**, 28759–28766 (2016).

[40] A. Bafekry, M. Ghergherehchi, and S. Farjami Shayesteh, "Tuning the electronic and magnetic properties of antimonene nanosheets via point defects and external fields: First-principles calculations," Phys. Chem. Chem. Phys. **21**, 10552–10566 (2019).

[41] A. Ramasubramaniam and D. Naveh, Mn-doped monolayer MoS_2: An atomically thin dilute magnetic semiconductor," Phys. Rev. B **87**, 195201 (2013).

[42] S. R. Naqvi, T. Hussain, W. Luo, and R. Ahuja, "Exploring doping characteristics of various adatoms on single-layer stanene," J. Phys. Chem. C **121**, 7667–7676 (2017).

[43] A. Bafekry, B. Mortazavi, and S. F. Shayesteh, "Band gap and magnetism engineering in Dirac half-metallic Na_2C nanosheet via layer thickness, strain and point defects," J. Magn. Magn. Mater. **491**, 165565 (2019).

[44] M. Yagmurcukardes, "Monolayer fluoro-InSe: Formation of a thin monolayer via fluorination of InSe," Phys. Rev. B **100**, 024108 (2019).

[45] D. Gao, S. Shi, K. Tao, B. Xia, and D. Xue, "Tunable ferromagnetic ordering in MoS_2 nanosheets with fluorine adsorption," Nanoscale **7**, 4211–4216 (2015).

[46] A. Bafekry, C. Stampfl, M. Ghergherehchi, and S. Farjami Shayesteh, "A first-principles study of the effects of atom impurities, defects, strain, electric field and layer thickness on the electronic and magnetic properties of the C_2N nanosheet," Carbon **157**, 371–384 (2020).

[47] B. Akgenc, "New predicted two-dimensional MXenes and their structural, electronic and lattice dynamical properties," Solid State Commun. **303–304**, 113739 (2020).

[48] A. Bafekry, M. Ghergherehchi, and S. Farjami Shayesteh, "Tuning the electronic and magnetic properties of antimonene nanosheets via point defects and external fields: first-principles calculations," Phys. Chem. Chem. Phys. **21**, 10552–10566 (2019).

[49] D. Kiymaz, M. Yagmurcukardes, A. Tomak, H. Sahin, R. T. Senger, F. M. Peeters, H. M. Zareie, and C. Zafer, "Controlled growth mechanism of poly (3-hexylthiophene) nanowires," Nanotechnology **27**, 455604 (2016).

[50] A. Bafekry, B. Akgenc, S. Farjami Shayesteh, and B. Mortazavi, "Tunable electronic and magnetic properties of graphene/carbon-nitride van der Waals heterostructures," Appl. Surf. Sci. 144450 (2019).

[51] Z. Kahraman, A. Kandemir, M. Yagmurcukardes, and H. Sahin, "Single-layer Janus-type platinum dichalcogenides and their heterostructures," J. Phys. Chem. C **123**, 4549–4557 (2019).

[52] A. Bafekry, S. Farjami Shayesteh, M. Ghergherehchi, and F. M. Peeters, "Tuning the bandgap and introducing magnetism into monolayer BC_3 by strain/defect engineering and adatom/molecule adsorption," J. Appl. Phys. **126**, 144304 (2019).

[53] M. Yagmurcukardes, S. Ozen, F. Iyikana, F. M. Peeters, and H. Sahin, "Raman fingerprint of stacking order in HfS_2-$Ca(OH)_2$ heterobilayer," Phys. Rev. B **99**, 205405 (2019).

[54] A. Bafekry, C. Stampfl, and S. Shayesteh, "A first-principles study of C_3N nanostructures: Control and engineering of the electronic and magnetic properties of nanosheets, tubes and ribbons," ChemPhysChem (2019).

[55] S. V. Badalov, M. Yagmurcukardes, F. M. Peeters, and H. Sahin, "Enhanced stability of single-layer w-gallenene through hydrogenation," J. Phys. Chem. C **122**, 28302–28309 (2018).

[56] S. V. Badalov, M. Yagmurcukardes, F. M. Peeters, and H. Sahin, "Enhanced stability of single-layer w-gallenene through hydrogenation," J. Phys. Chem. C **122**, 28302–28309 (2018).

[57] S. Chintalapati, L. Shen, Q. Xiong, and Y. P. Feng, "Magnetism in phosphorene: Interplay between vacancy and strain," Appl. Phys. Lett. **107**, 072401 (2015).

[58] A. Bafekry, C. Stampfl, S. F. Shayesteh, and F. M. Peeters, "Exploiting the novel electronic and magnetic structure of C_3N via functionalization and conformation," Adv. Electr. Mater. (published online).

[59] M. Yagmurcukardes, C. Bacaksiz, R. T. Senger, and H. Sahin, "Hydrogen-induced structural transition in single layer ReS_2," 2D Mater. **4**, 035013 (2017).

[60] T. Ozaki, K. Nishio, and H. Kino, "Efficient implementation of the nonequilibrium Green function method for electronic transport calculations," Phys. Rev. B **81**, 035116 (2010).

[61] J. P. Perdew, K. Burke, and M. Ernzerhof, "Generalized gradient approximation made simple," Phys. Rev. Lett. **77**, 3865–3868 (1996).

[62] N. Troullier and J. L. Martins, "Efficient pseudopotentials for plane-wave calculations," Phys. Rev. B **43**, 1993–2006 (1991).

[63] T. Ozaki, "Variationally optimized atomic orbitals for large-scale electronic structures," Phys. Rev. B **67**, 155108 (2003).

[64] T. Ozaki and H. Kino, "Numerical atomic basis orbitals from H to Kr," Phys. Rev. B **69**, 195113 (2004).

[65] H. J. Monkhorst and J. D. Pack, "Special points for Brillouin-zone integrations," Phys. Rev. B **13**, 5188–5192 (1976).

[66] J. Tersoff and D. R. Hamann, "Theory and application for the scanning tunneling microscope," Phys. Rev. Lett. **50**, 1998–2001 (1983).

[67] I. Horcas, R. Fernández, J. M Gómez-Rodríguez, J. Colchero, J. Gómez-Herrero, and A. M. Baro, "WSXM: A software for scanning probe microscopy and a tool for nanotechnology," Rev. Sci. Instrum. **78**, 013705 (2007).

[68] L. Zhu, Q. Xue, X. Li, T. Wu, Y. Jin, and W. Xing, "C_2N: An excellent two-dimensional monolayer membrane for He separation," J. Mater. Chem. A **3**, 21351–21356 (2015).

[69] Y. Qu, F. Li, H. Zhou, and M. Zhao, "Highly efficient quantum sieving in porous graphene-like carbon nitride for light isotopes separation," Sci. Rep. **6**, 19952 (2016).

[70] H. Xu, H. Xiang, Q. Wei, J. Q. Liu, Y. D. Xia, J. Yin, and Z. G. Liu, "Two-dimensional graphene-like C_2N: An experimentally available porous membrane for hydrogen purification," Phys. Chem. Chem. Phys. **17**, 15115–15118 (2015).

[71]I. Choudhuri and B. Pathak, "Ferromagnetism and half-metallicity in atomically thin holey nitrogenated graphene based systems," Chem. Phys. Chem. **18**, 2336–2346 (2107).

[72]D. Mpoutas and L. Tsetseris, "Magnetic two-dimensional C_3N_2 carbonitrides: Semiconductors, metals and half-metals," Phys. Chem. Chem. Phys. **19**, 26743–26748 (2017).

[73]L. Tsetseris, "Functionalization of two-dimensional phthalo-carbonitride with metal atoms," Phys. Chem. Chem. Phys. **18**, 26088–26093 (2016).

[74]E. Kroke, M. Schwarz, E. Horath-Bordon, P. Kroll, B. Noll, and A. D. Norman, "Tri-s-triazine derivatives. Part I. From trichloro-tri-s-triazine to graphitic C_3N_4 structures," New J. Chem. **26**, 508–512 (2002).

[75]X. Wang, K. Maeda, A. Thomas, K. Takanabe, G. Xin, J. M. Carlsson, K. Domen, and M. Antonietti, "A metal-free polymeric photocatalyst for hydrogen production from water under visible light," Nat. Mater. **8**, 76–80 (2008).

[76]G. Liu, P. Niu, S. C. Smith, Zh. Chen, G. Q. (Max) Lu, and H.-M. Cheng, "Unique electronic structure induced high photoreactivity of sulfur-doped graphitic C_3N_4," J. Am. Chem. Soc. **132**, 11642–11648 (2010).

[77]K. Srinivasu, B. Modak, and S. K. Ghosh, "Porous graphitic carbon nitride: A possible metal-free photocatalyst for water splitting," J. Phys. Chem. C **118**, 26479–26484 (2014).

[78]J. Wirth, R. Neumann, M. Antonietti, and P. Saalfrank, "Adsorption and photocatalytic splitting of water on graphitic carbon nitride: A combined first principles and semiempirical study," Phys. Chem. Chem. Phys. **16**, 15917–15926 (2014).

[79]I. Choudhuri, G. Bhattacharyya, S. Kumar, and B. Pathak, "Metal-free half-metallicity in a high energy phase C-doped gh-C_3N_4 system: A high curie temperature planar system," J. Mater. Chem. C **4**, 11530–11539 (2016).

[80]S. Sarikurt and F. Ersan, "Phononic stability analysis of two-dimensional carbon nitride monolayers," Marmara J. Pure Appl. Sci. **30**(4), 383–387 (2018).

[81]H. Chen, Sh. Zhang, W. Jiang, Ch. Zhang, H. Guo, Zh. Liu, Zh. Wang, F. Liu, and X. Niu, "Prediction of two-dimensional nodal-line semimetals in a carbon nitride covalent network," J. Mater. Chem. A **6**, 11252–11259 (2018).

[82]H. Li, H. Hu, Ch. Bao, J. Hua, H. Zhou, X. Liu, X. Liu, and M. Zhao, "Tensile strain induced half-metallicity in graphene-like carbon nitride," Phys. Chem. Chem. Phys. **17**, 6028–6035 (2015).

[83]X. Zhang and M. Zhao, "Prediction of quantum anomalous Hall effect on graphene nanomesh," RSC Adv. **5**, 9875–9880 (2015).

[84]X. Zhang, A. Wang, and M. Zhao, "Spin-gapless semiconducting graphitic carbon nitrides: A theoretical design from first principles," Carbon **84**, 1–8 (2015).

[85]L. L. Li, X. Kong, O. Leenaerts, X. Chen, B. Sanyal, and F. M. Peeters, "Carbon-rich carbon nitride monolayers with Dirac cones: Dumbbell C_4N," Carbon **118**, 285–290 (2017).

[86]A. H. Castro Neto, F. Guinea, N. M. R. Peres, K. S. Novoselov, and A. K. Geim, "The electronic properties of graphene," Rev. Mod. Phys. **81**, 109–162 (2009).

[87]K. S. Novoselov, D. Jiang, F. Schedin, T. J. Booth, V. V. Khotkevich, S. V. Morozov, and A. K. Geim, "Two-dimensional atomic crystals," Proc. Natl. Acad. Sci. U.S.A. **102**, 10451–10453 (2005).

[88]Y. Li, Z. Zhou, G. Yu, W. Chen, and Z. Chen, "CO catalytic oxidation on iron-embedded graphene: Computational quest for low-cost nanocatalysts," J. Phys. Chem. C **114**, 6250–6254 (2010).

[89]A. K. Geim and K. S. Novoselov, "The rise of graphene," Nat. Mater. **6**(3), 183–191 (2007).

[90]M. Yagmurcukardes, S. Horzum, E. Torun, F. M. Peeters, and R. Tugrul Senger, "Nitrogenated, phosphorated and arsenicated monolayer holey graphenes," Phys. Chem. Chem. Phys. **18**, 3144–3150 (2016).

[91]R. Zhang, B. Li, and J. Yang, "Effects of stacking order, layer number and external electric field on electronic structures of few-layer C_2N-h2D," Nanoscale **7**, 14062–14070 (2015).

[92]Q. Hu, Q. Wu, H. Wang, J. He, and G. Zhang, "First-principles studies of structural and electronic properties of layered C_3N phases," Phys. Status Solidi (b) **249**, 784–788 (2011).

[93]H. J. Xiang, B. Huang, Z. Y. Li, S.-H. Wei, J. L. Yang, and X. G. Gong, "Ordered semiconducting nitrogen-graphene alloys," Phys. Rev. X **2**, 011003 (2012).

[94]H. Wu, Y. Liu, E. Kan, W. Xu, J. Li, M. Yan, R. Lu, J. Wei, Y. Qian, and Y. Ma, "The diverse electronic properties of C_4N_3 monolayer under biaxial compressive strain: A theoretical study," Appl. Phys. **49**, 295301 (2016).

[95]X. Li, Y. Dai, Y. Ma, Sh. Han, and B. Huang, "Graphene/g-C_3N_4 bilayer: Considerable band gap opening and effective band structure engineering," Phys. Chem. Chem. Phys. **16**, 4230–4235 (2014).

[96]O. Leenaerts, H. Peelaers, A. D. Hernández-Nieves, B. Partoens, and F. M. Peeters, "First-principles investigation of graphene fluoride and graphane," Phys. Rev. B **82**, 195436 (2010).

[97]M. M. Ugeda, I. Brihuega, F. Guinea, and J. M. Gómez-Rodríguez, "Missing atom as a source of carbon magnetism," Phys. Rev. Lett. **104**, 096804 (2010).

[98]H. A. Jahn and E. Teller, "Stability of polyatomic molecules in degenerate electronic states-I—Orbital degeneracy," Proc. R. Soc. London A **161**, 220–235 (1937).